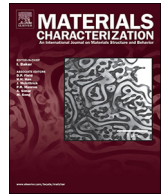




ELSEVIER

Contents lists available at ScienceDirect

Materials Characterization

journal homepage: www.elsevier.com/locate/matchar

Microstructure and functionality of a uniquely graded super duplex stainless steel designed by a novel arc heat treatment method

Vahid A. Hosseini^{a,b,*}, Leif Karlsson^a, Cem Örnek^{c,d}, Pierfranco Reccagni^e, Sten Wessman^a, Dirk Engelberg^e

^a Department of Engineering Science, University West, SE-461 86 Trollhättan, Sweden

^b Innovatum AB, Trollhättan, SE-461 29 Trollhättan, Sweden

^c Department of Chemical Science and Engineering, Division of Surface and Corrosion Science, KTH Royal Institute of Technology, SE-100 44 Stockholm, Sweden

^d Department of Corrosion in Energy and Processing Industry, Swerea KIMAB AB, P.O. Box 7047, SE-164 40 Kista, Sweden

^e School of Materials, The University of Manchester, Manchester M13 9PL, UK

ARTICLE INFO

Keywords:

Functionally graded microstructure
Sigma phase
475 °C-embrittlement
Chi phase
R-phase
Nitrogen loss

ABSTRACT

A novel arc heat treatment technique was applied to design a uniquely graded super duplex stainless steel (SDSS), by subjecting a single sample to a steady state temperature gradient for 10 h. A new experimental approach was used to map precipitation in microstructure, covering aging temperatures of up to 1430 °C. The microstructure was characterized and functionality was evaluated via hardness mapping. Nitrogen depletion adjacent to the fusion boundary depressed the upper temperature limit for austenite formation and influenced the phase balance above 980 °C. Austenite/ferrite boundaries deviating from Kurdjumov–Sachs orientation relationship (OR) were preferred locations for precipitation of σ at 630–1000 °C, χ at 560–1000 °C, Cr_2N at 600–900 °C and R between 550 °C and 700 °C. Precipitate morphology changed with decreasing temperature; from blocky to coral-shaped for σ , from discrete blocky to elongated particles for χ , and from polygonal to disc-shaped for R. Thermodynamic calculations of phase equilibria largely agreed with observations above 750 °C when considering nitrogen loss. Formation of intermetallic phases and 475 °C-embrittlement resulted in increased hardness. A schematic diagram, correlating information about phase contents, morphologies and hardness, as a function of exposure temperature, is introduced for evaluation of functionality of microstructures.

1. Introduction

Super duplex stainless steels (SDSS) offer excellent mechanical properties with high corrosion resistance and are superior to most of their ferritic and austenitic counterparts due to the synergy between ferrite (δ) and austenite (γ) in the duplex microstructure [1–3]. Optimum properties of SDSS have been reported for balanced ratios of ferrite and austenite allowing production of high-performance materials with low wall thickness and light weight [4]. However, material processing practices, such as welding, cutting, and aging, or excessive service temperatures can cause microstructure degradation due to phase separation reactions occurring at temperatures intervals between ca. 250–1000 °C [1,5]. Intermetallic phases, such as sigma (σ), chi (χ), G, R, nitrides and carbides can form which then often lead to a reduction of the optimum microstructure balance, resulting in embrittlement and sensitization [6–8]. Ferrite decomposition into Cr-rich (α) and Fe-rich (α') region results in 475 °C-embrittlement, typically

accompanied with a reduction in toughness and an increase in hardness [9,10]. Getting a complete picture of the transformation behavior therefore requires a study of specimens heat-treated over a wide range of temperatures.

The most deleterious intermetallic precipitation at temperatures of around 600–1000 °C in duplex stainless steel is σ -phase, which significantly decreases the toughness and pitting corrosion resistance [1,5]. Another important intermetallic is χ -phase, which has a cubic crystallography lattice, easily precipitates at δ/γ phase boundaries, and often has been associated as a potential nucleation site for σ -phase [1,6]. Different nitrides, including Cr_2N , CrN, and Pi-nitride (π) may also form and result in Cr depletion in their vicinity [2,11]. R phase is enriched in Mo and Si [12] and is also known to decrease toughness significantly [13].

Phase transformations in SDSS have often been studied by conventional furnace or salt bath heat treatments, by producing time-temperature-precipitation (TTP) and continuous cooling transformation

* Corresponding author at: Department of Engineering Science, University West, SE-461 86 Trollhättan, Sweden.

E-mail addresses: vahid.hosseini@hv.se (V. A. Hosseini), leif.karlsson@hv.se (L. Karlsson), ornek@kth.se (C. Örnek), pierfranco.reccagni@postgrad.manchester.ac.uk (P. Reccagni), sten.wessman@swerea.se (S. Wessman), D.Engelberg@manchester.ac.uk (D. Engelberg).

<https://doi.org/10.1016/j.matchar.2018.03.024>

Received 25 November 2017; Received in revised form 23 February 2018; Accepted 18 March 2018

Available online 19 March 2018

1044-5803/ © 2018 The Authors. Published by Elsevier Inc. This is an open access article under the CC BY-NC-ND license (<http://creativecommons.org/licenses/by-nc-nd/4.0/>).

(CCT) diagrams. These require extensive experiment time to be generated. Recently, Hosseini et al. [14] developed a novel arc-heat treatment method, capable of producing a wide range of aging temperatures in a single test specimen, showing that reliable and reproducible steady-state temperature gradients can be achieved within a few seconds and sustained for several hours. The technique was recently employed to study the phase transformations occurring in super duplex weld metal heat treated for 1 min or 10 min, where practical time-temperature precipitation and property diagrams were produced [15]. In the present study, however, this technique was employed to produce a functionally graded SDSS microstructure to facilitate material characterization over a range of temperatures for a much longer heat treatment time (10 h).

Different methods may be employed to characterize microstructures, although only a few can be used both for phase identification and studies of crystallographic orientation relationships. Transmission electron microscopy is capable of both, but each specimen only covers a small area, which makes it difficult and time-consuming to apply to graded microstructures. Electron backscattered diffraction (EBSD), on the other hand, is a technique that can be used to map larger areas. Recently, Örnek et al. [11] showed that EBSD can also be used to study precipitated phases with the size of 500 nm and smaller in a duplex stainless steel. This method is therefore particularly well suited for studies of a graded microstructure to understand crystallographic development as well as the effect of local stress/strain conditions on component performance [10,16–19].

Numerous studies of the microstructure development of super duplex stainless steels exist in the literature, for temperatures between about 400–1000 °C [2,20]. However, these do not specifically show the gradual change of the microstructure with temperature in a single specimen, which has more practical relevance in assessing heat affected structural components. In the present study, a full set of functionally graded microstructures are obtained and characterized, which aims to address an important knowledge gap for the precipitation behavior of 2507 SDSS microstructures, and their path towards equilibrium conditions for a wide range of annealing temperatures. Nitrogen loss from the weld pool is known to occur during welding of duplex stainless steel, as studied by Hosseini et al. [21]. However, it is rarely considered to affect the high temperature heat affected zone (HT-HAZ). The present study, however, reports on depletion by solid state diffusion of nitrogen and its influence on the ferrite/austenite balance adjacent to the fusion boundary. A novel arc heat treatment technique was applied to produce structurally and functionally graded microstructures in a single sample. EBSD, x-ray diffraction and microhardness analyses were used for microstructure characterization and property assessment and the microstructure development was compared to thermodynamic calculations and simulations using Thermo-Calc and JMatPro.

2. Experimental

2.1. Material

A grade 2507 SDSS (EN: 1.4410, UNS S32750) from Outokumpu Stainless AB, Sweden, delivered as a plate material in 6 mm thickness, was used in this study. The chemical composition of the plate is listed in Table 1. The plate material was in a hot-rolled, solution-annealed condition and is denoted as as-received in this paper. Disc shaped specimens with a diameter of 99 mm were manufactured.

An arc heat treatment technique, described in detail in Ref. [14], was used to produce a graded microstructure. The arc heat treatment

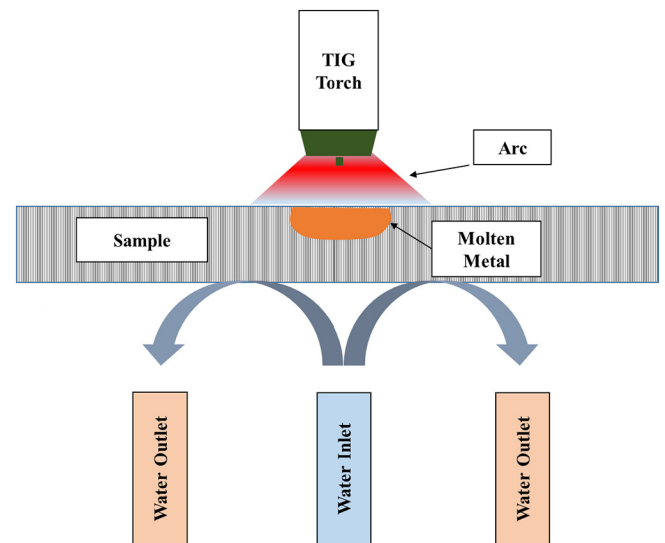


Fig. 1. Schematic illustration of arc heat treatment technique. A stationary arc was applied to a plate mounted on a water-cooled chamber.

device includes a water cooled chamber and a stationary tungsten inert-gas (TIG) gun. The disc was mounted in the device and exposed to a stationary TIG arc for 10 h in argon gas environment. The applied current and arc length were 100 A and 3 mm, respectively. The arc was placed in the center of the disc to get a symmetric heat distribution during the heat treatment. This produced a continuous, steady state, temperature gradient resulting in a functionally graded microstructure heat-treated from the liquidus temperature at the border of the weld pool to approximately 13 °C on the back side of the sample, governed by the cooling water temperature (Fig. 1). Thermocouples were attached to the top and back-side of the disc, with the temperature measured to provide data for temperature distribution simulations. The steady state condition was achieved after 11 s, and cooling to ambient temperature took 7 s, suggesting heating and cooling times were negligible compared to the 10 h steady state heat treatment.

One additional coupon specimen was furnace heat treated at 475 °C for 10 h, to investigate a region of increased hardness and different etching response of the arc heat treatment sample.

2.2. Microstructure Characterization

The arc heat treated disc was waterjet-cut to prevent any further exposure to heating, and cross sections were ground and polished to a 1/4 μm diamond paste finish, followed by OP-S polishing for scanning electron microscopy (SEM), energy dispersive X-ray spectrometry (EDS), and EBSD analysis. The cross-section was chemically etched using (i) a modified Beraha's etchant (60 ml H₂O, 30 ml HCL, 0.5 g K₂S₂O₅) to reveal the location of the fusion zone, and (ii) electro-chemically etched with 10% NaOH at a voltage of 4 V for 6 s, to reveal the ferrite. Optical images of the etched samples were obtained with an Olympus BX60M optical microscope.

A TM3000 Toshiba scanning electron microscope (SEM) equipped with an EDS detector was used to get an overview of crystallographic phases of the OP-S polished sample. The content of nitrogen, chromium and nickel were measured in the vicinity of the fusion zone by a JEOL JSM-7000F field emission gun (FEG) SEM, equipped with an INCA WAVE Wavelength Dispersive x-ray Spectrometer (WDS).

EBSD analysis of regions heat treated at temperatures in excess of 750 °C was performed with a FEI Quanta 650 FEG-SEM equipped with a Nordlys EBSD detector from Oxford Instruments and AZtec 2.2 acquisition software. An acceleration voltage of 20 kV and step sizes between 100 and 700 nm were used, yielding indexing rates better than > 88%.

Regions exposed to temperature of 750 °C and below were analyzed

Table 1
Chemical composition (wt%) of 2507 SDSS.

C	Si	Mn	P	S	Cr	Ni	Mo	N	Cu	Fe
0.016	0.44	0.76	0.028	0.001	25.04	6.93	3.78	0.265	0.40	Bal.

using the high-resolution FEI Magellan SEM, equipped with a Nordlys EBSD detector from Oxford Instruments with AZtec 2.2 acquisition software. EBSD mapping was performed with a step size of 54 nm with 10 kV to index smaller precipitates [11]. A minimum of 6 Kikuchi patterns were set for phase identification and EBSD data were evaluated with HKL Channel 5 post processing to obtain the content of different phases, crystallographic orientation relationships, and information about the austenite spacing using the a Mean Linear Intercept (MLI) method.

XRD was used to support phase identification in the as received microstructure, as well as all arc heat treated regions in the temperature range 400–1200 °C. A Bruker D8 Discover with a Co-K α X-ray source ($k = 1.78901 \text{ \AA}$) was employed with following parameters: 40 mA, 35 kV, $2\theta = 45^\circ\text{--}114^\circ$, a 2θ scan step size of 0.02°, exposure time of 2.6 s for each step, and a spot diameter of 200 μm .

Microhardness testing was carried out to study the influence of arc heat treatment at different temperature using the Struers DuraScan 80 automated hardness tester. A microhardness map of the cross section was generated following ASTM E384-10 standard. An indenter load of 200 g with a dwelling time of 15 s was used with 1272 indents in total. In addition, to measure the hardness in ferrite and austenite of the furnace-aged sample, an indenter load of 25 g was used, resulting in typical indentations of 7–10 μm .

2.3. Modeling of Temperature Distribution and Thermodynamic Calculations

Temperature simulations were used to estimate the temperature distribution through the cross section of the arc treated sample. OpenFOAM® software was used, with the actual geometry of the fusion boundary, measured in the cross section of the arc heat-treated sample, and steady state temperatures recorded via the attached thermocouple defined as boundary conditions. Temperature dependent thermodynamic and transport properties including thermal conductivity (18–34 W/(m·K)), specific heat (0.46–1.07 J/(g·K)), and density (7.3–7.8 g/cm $^{-3}$) were extracted from JMatPro for the material composition. The conductive heat transfer equation was used to estimate the temperature distribution in the arc heat-treated sample. A mesh consisting of 20,200 quadrilaterals elements was employed for the modeling. A detailed description of the modeling has been reported in [14,22].

Thermo-Calc software with TCFE8 database was used to calculate equilibrium phase fractions from 400 °C to 1500 °C. Equilibrium phase fractions were calculated for different nitrogen contents as nitrogen loss was observed next to the fusion boundary. The JMatPro software package V6.2.1 was employed to obtain supporting information for comparison. However, it should be noted that equilibrium conditions require longer heat treatments than the reported 10 h exposure here, especially in the lower temperature regime. Therefore, the calculated and measured absolute phase fractions should be considered as approximations.

3. Results

3.1. Temperature Distribution and Microstructures

The calculated temperature distribution and macrostructure of the heat treated sample are shown in Fig. 2. Nine regions were defined based on the microstructure and temperature range in each region, which are highlighted in the temperature distribution map (regions 1–9). An EBSD phase map, showing the full spectrum of graded microstructures, is presented in Fig. 3, and representative SEM micrographs from the different regions, corresponding to different heat treatment temperatures, are shown in Fig. 4. A brief description of the different microstructure regions is summarized below.

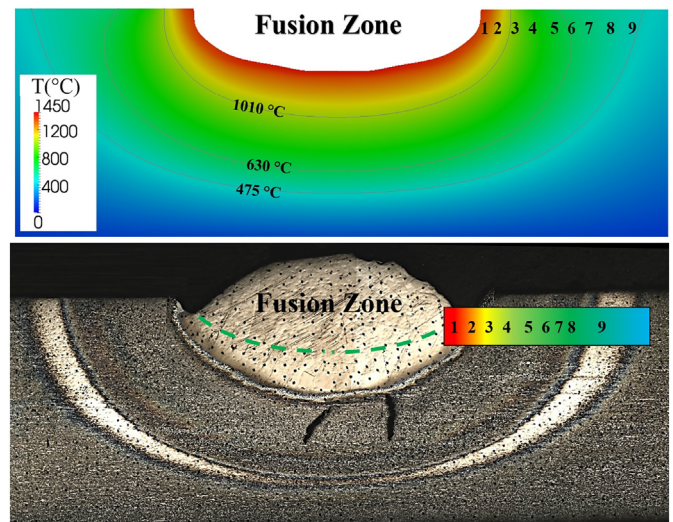


Fig. 2. Simulated temperature field map (top) and cross section (bottom) of the functionally graded SDSS sample arc heat treated for 10 h. The microstructure was analyzed in the numbered regions and correlated with calculated temperatures profiles.

- **Fusion zone:** $T >$ liquidus ($> 1430 \text{ }^\circ\text{C}$). Material was in the molten state during arc heat treatment and solidified on cooling after arc heat treatment. This zone has a fully ferritic microstructure.
- **Region 1 (R1):** 1150–1430 °C, where the microstructure is fully ferritic (Fig. 3). This region was not melted during arc heat treatment.
- **Region 2 (R2):** 1010–1150 °C. Only austenite and ferrite are present.
- **Region 3 (R3):** 950–1010 °C. Ferrite, austenite and σ are the major phases with some traces of χ . Fig. 4 shows how σ first appears at around 1010 °C.
- **Region 4 (R4) and region 5 (R5):** 800–930 °C and 670–790 °C, respectively. Austenite and σ are the major phases as shown in Fig. 4. Other phases are also present in the microstructure.
- **Region 6 (R6):** 630–660 °C, contains austenite, ferrite, σ , χ , R, thin films and nitrides.
- **Region 7 (R7):** 560–630 °C, where σ is no longer seen in the microstructure but R, χ , thin films (indicated by “?” in Fig. 4) and nitrides were observed.
- **Region 8 (R8):** 500–560 °C, where no secondary phases were observed.
- **Region 9 (R9):** 400–500 °C, where no secondary phases were seen, but the etching response was different from that of the unaffected base metal.

3.2. Nitrogen Loss

The chemical composition was measured across the fusion boundary to provide input for calculating equilibrium phase diagrams (Fig. 5a). Chemical analyses showed that chromium and nickel contents were stable, only varying within 27.5–28.7 wt% and 7.0–7.4 wt%, respectively. However, Fig. 5b also shows that nitrogen was depleted up to a distance of approximately 1.2 mm away from the fusion boundary, corresponding to temperatures from the liquidus point to a temperature of 980 °C along the measurement line. The nitrogen content within the first 1.1 mm from the fusion boundary was therefore considered to be zero in the thermodynamic calculations.

3.3. Phase Identification

Table 2 summarizes thermodynamically predicted and observed secondary phases via SEM and EBSD analyses. The phase equilibrium above 980 °C was calculated assuming a nitrogen free alloy and below 980 °C using the as-received nitrogen content in Table 1. In general, the calculations showed that JMatPro predicts a greater number of phases than Thermo-Calc. In addition to ferrite and austenite, σ , χ , Cr $_2$ N and R were found in the microstructure in different regions. The EDS spectra showing detected elemental peaks for σ , χ , and R as well as γ and δ are presented in Fig. 6, where the ratios of Mo to Fe peak heights are ranked as follows: R, χ , σ , δ , and γ . The higher ratio of Mo to Fe peak heights suggests higher content of Mo, also confirmed by the stronger BSE imaging contrast in the SEM. The result is in good agreement with the

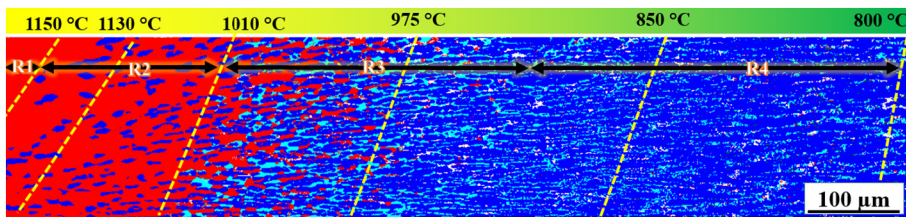


Fig. 3. EBSD phase map showing the graded microstructure after 10 h arc heat treatment. Dashed lines (yellow) indicate isotherms. Ferrite (red), austenite (blue), and σ (aqua) are shown. The image covers regions 1–4. (For interpretation of the references to color in this figure legend, the reader is referred to the web version of this article.)

study of Nilsson et al. [2], where the same trend of Mo content in R, χ , and σ for 2507 SDSS was reported.

Furthermore, decomposition of the ferrite into α' and α was concluded to have occurred for temperatures around 475 °C [23]. A detailed discussion about the observed phases in Table 2 is presented in the following sections.

3.4. Comparison of Modeled Vs. Measured Phase Fractions

Table 3 lists predicted and measured phase contents at different temperatures. The ferrite/austenite ratio was $50/50 \pm 2$ in the unaffected material. As seen in Fig. 3 and, a fully ferritic region formed in the fusion zone and in HAZ down to 1150 °C (R1). JMatPro and Thermo-Calc also predicted this to occur for a nitrogen free alloy down to temperatures of 1180 °C and 1170 °C, respectively, which is in good agreement with observation. It therefore supports the assumption of complete nitrogen depletion next to the fusion boundary. The ferrite content gradually decreased with lowering the temperature, and was found to be < 1% between 750 °C and 880 °C. The ferrite content then gradually increased with decreasing temperature to the unaffected material ferrite content of 50%. Between 980 °C and 1000 °C, ferrite content was lower than predicted by Thermo-Calc, which is the temperature threshold from where significant nitrogen depletion occurred (Fig. 5b).

Table 3 shows good agreement between measured and Thermo-Calc predicted austenite contents down to temperatures of 750 °C. The austenite content increased with decreasing temperature until 880 °C, reaching a maximum content of 71%. There was a sudden change in the austenite content around 990 °C. At 980 °C, with the measured austenite content right between values predicted for nitrogen containing and nitrogen-free SDSS compositions. Interestingly at 640 °C, the measured austenite content was higher than both the initial and calculated contents; however, around 7% ferrite was still present in the microstructure (Table 3), which implies a non-equilibrium condition for the phase balance.

Between 630 and 1000 °C, σ -phase was found (Table 2), with a maximum content of 34.4% at 750 °C, showing good agreement with calculations, between 750 and 880 °C. However, differences between phase fraction measurements and Thermo-Calc predictions were

observed for temperatures above 950 °C and below 750 °C. Above 950 °C, the content of σ -phase was much higher than predicted by Thermo-Calc. Below 750 °C, on the other hand, the calculated σ -phase fraction was much lower than the measured fraction, with measured contents about 14% and 20% higher than the equilibrium content at 650 °C and 640 °C, respectively.

Small amounts of χ -phase were present in the microstructure between approximately 580 °C and 1000 °C, with a maximum of $\approx 1.1\%$ at 640 °C (Table 3). The presence of R-phase was also found in the microstructure at temperatures below 700 °C, but the content of R + χ + thin film did not exceed 2.3%.

3.5. Functionally Graded Microstructure

The key characteristics of observed crystallographic phases present in the graded microstructure are explained. Fig. 7a shows an EBSD phase map for 1010–1090 °C (R2), where the microstructure contains only austenite and ferrite and no secondary phases were detected. The austenite spacing increased from $1.2 \pm 1.0 \mu\text{m}$ in the unaffected material to $12.1 \pm 9.2 \mu\text{m}$ in R2.

Secondary austenite forms together with secondary phases, particularly with σ -phase, consuming the ferrite as shown in Fig. 7b. The grain orientation map in Fig. 7d shows that γ_2 forms right next to σ -particles (arrows 1 and 2) and epitaxially grew along primary austenite grains. However, in some cases it was observed that ferrite transformed into σ -phase without formation of γ_2 (arrow 3). In this case, σ -phase grew on the δ/γ boundary into δ . Fig. 4 shows changes in σ -phase morphology as a function of temperature, going from blocky precipitates above ≈ 900 °C, to coral-like shapes at lower temperatures. Preferred locations of σ -phase were ferrite/austenite phase boundaries, further growing into ferritic regions. In particular at lower temperatures this was accompanied by the formation of finer secondary austenite as seen in Fig. 8(a & b).

Above 670 °C, χ -phase precipitates were mostly seen as particles on δ/γ phase boundaries, as shown for regions 3–5 in Fig. 4. Below 700 °C, χ was found at δ/γ boundaries and also as elongated particles at γ/σ boundaries (Fig. 8a and e), inside σ -phase (Fig. 8b and f) and at previous δ/γ phase boundaries, together with Cr_2N (Fig. 8d and h).

Some further constituents, noticeable from their bright contrast in

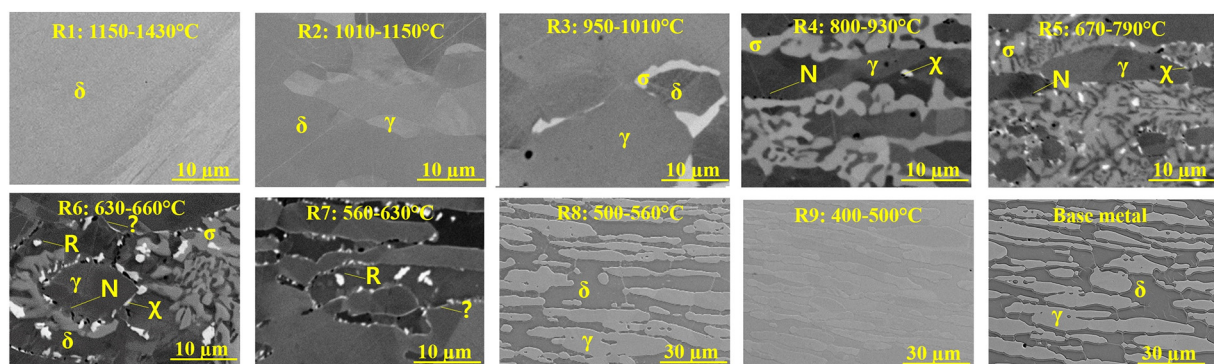


Fig. 4. Representative back scattered electron (BSE) SEM micrographs of graded microstructures from regions defined in the cross section in Fig. 1, showing ferrite (δ), austenite (γ), sigma phase (σ), chi phase (χ), nitrides (N), thin film (?) and R-phase (R) present within the different regions (T-R9).

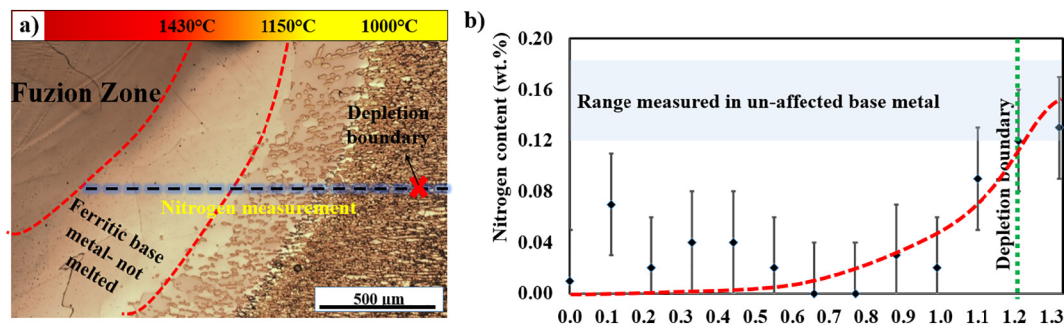


Fig. 5. a) Microstructure of the fusion boundary with dashed black line showing where the chemical compositions were measured. The left line shows the fusion boundary and the right the end of the fully ferritic region. b) WDS measurements of the nitrogen content next to the fusion boundary showing nitrogen loss until 1.2 mm from the fusion boundary.

Table 2

Predicted and observed secondary phases in the 10 h arc heat treated sample (LOM = Light Optical Microscopy).

Region	Temp. (°C)	Predicted		Observed	
		JMatPro	Thermo-Calc	XRD	LOM/SEM/EDS/EBSD
1	1150–1430	–	–	–	–
2	1010–1150	σ	–	σ, χ	–
3	950–1010	σ	σ	σ, χ	σ, χ
4	800–930	$\sigma, \text{Cr}_2\text{N}, \chi, \text{M}_{23}\text{C}_6$	$\sigma, \text{Cr}_2\text{N}, \text{M}_{23}\text{C}_6$	$\sigma, \text{Cr}_2\text{N}, \sigma, \chi, \text{Cr}_2\text{N}$	$\sigma, \chi, \text{Cr}_2\text{N}$
5	670–790	$\sigma, \text{Laves}, \text{Cr}_2\text{N}, \chi, \text{M}_{23}\text{C}_6$	$\sigma, \text{Cr}_2\text{N}, \text{M}_{23}\text{C}_6$	$\sigma, \chi, \text{Cr}_2\text{N}, \text{Cr}_2\text{N}, \text{R}?$	$\text{Cr}_2\text{N}, \chi, \text{R}?$
6	630–660	$\sigma, \text{Laves}, \text{Cr}_2\text{N}, \text{M}_{23}\text{C}_6$	$\sigma, \text{Cr}_2\text{N}, \text{M}_{23}\text{C}_6$	R	$\text{Cr}_2\text{N}, \chi, \text{R}$, thin film
7	560–630	$\sigma, \text{Laves}, \text{Cr}_2\text{N}, \pi, \text{M}_{23}\text{C}_6$	$\sigma, \text{Cr}_2\text{N}, \text{M}_{23}\text{C}_6$	–	Nitrides, χ, R , thin film
8	500–560	$\sigma, \text{Laves}, \text{Cr}_2\text{N}, \pi, \text{G}, \text{Cu}, \text{M}_{23}\text{C}_6$	$\sigma, \text{Cr}_2\text{N}, \text{M}_{23}\text{C}_6$	–	–
9	400–500	$\alpha', \sigma, \text{Laves}, \gamma, \text{G}, \pi, \text{Cu}, \text{M}_{23}\text{C}_6$	$\sigma, \text{Cr}_2\text{N}, \text{M}_{23}\text{C}_6$	–	No selective etching of ferrite
BM		–	–	–	–

Note 1: The equilibrium phases were calculated for an alloy with 0% N for temperatures above 980 °C.

Note 2: “?” indicates that the phase could not be identified with confidence.

The BSE SEM images in regions 5–7, were located mostly inside the ferrite grains but, as shown in Fig. 8c, these could not be indexed by EBSD. The precipitates inside grains seemed to be disc-shaped growing in two perpendicular directions in region 7, and were enriched in Mo and Si, while depleted in Cr and Mn, as shown in Fig. 9. XRD analysis suggests that R-phase could be present in the regions 6 and 7, even though calculations via JMatPro and Thermo-Calc do not predict R to be a thermodynamically stable phase. The lowest temperature where R-phase was found was 560 °C and R was clearly distinguishable up to 660 °C. Its highest precipitation temperature, however, was not clear due to the similar contrast of R and χ particles. Particles with a similar morphology have been reported as R-phase in the literature for the same temperature range [17,18]. The current study suggests that R-phase has a blocky, irregular shape at higher temperatures, but is dis-shaped at lower temperatures.

Some very thin films also appeared at δ/δ and δ/γ boundaries in regions 6 and 7, as shown in Fig. 9. The contrast in BSE SEM and Mo distribution in the EDS elemental map, in Fig. 9a, suggest that these are enriched in Mo.

Nitrides formed between approximately 560 °C to 900 °C, mainly at ferrite/austenite interphase boundaries. Nitrides were also seen at σ/γ_2 boundaries. The XRD results summarized in Table 2, the SEM micrographs shown in Figs. 4, 8 and 9 (dark imaging precipitates), and the EBSD map shown in Fig. 8 detail the temperatures and locations where the nitrides were found. Calculations predicted the formation of both Cr_2N and π , but only Cr_2N could be identified.

3.6. Orientation Relationships

The orientation relationships between ferrite-austenite, ferrite- σ , and ferrite- χ are presented in Fig. 10, with a focus on regions 3 and 6, where both ferrite and σ -phase were present. The OR for austenite and ferrite was compared to Kurdjumov–Sachs (KS) orientation relationship ($(111)_\gamma // (110)_\delta$ and $[110]_\gamma // [111]_\delta$), which is known to be common for DSS [24]. Fig. 10a presents the deviation from KS OR in the as received base material and after heat treatment at 980–1010 °C (R3) and 640 °C (R6). Only a few boundaries were close to the KS OR in the base material, but a significant fraction had an OR within a few degrees of KS after the heat treatment in regions 3 & 6.

The OR between ferrite and σ -phase was compared to that suggested by Chen [25] ($(110)_\sigma // (1\bar{1}0)_\delta$ and $[332]_\sigma // [\bar{1}\bar{1}\bar{3}]_\delta$). As can be seen from Fig. 10b, only very few σ -ferrite boundaries were close to Chen's OR for regions 3 and 6. However, the non-random distribution of deviation angles could suggest that there might be another specific relationship between σ and δ .

EBSD analysis revealed that about half of χ -phase precipitates were within 2° of a cube-cube OR ($(001)_\delta // (001)_\chi$ and $[100]_\delta // [100]_\chi$) with adjacent ferrite grains [26].

3.7. Mechanical Properties

A microhardness map of the graded microstructure is shown in Fig. 11. Three distinctive regions with high hardness bands were apparent: (B1) hardness up to 480 HV0.2 for temperatures between 680 °C and 970 °C, associated with precipitation of σ , (B2) hardness of 320 HV0.2 temperatures between 590 and 630 °C where mainly R-phase precipitated, (B3) with a maximum hardness of 340 HV0.2 for temperatures between 450 °C and 480 °C, where a light etching band was observed by LOM (Fig. 2). The values measured in the present study are much higher than those reported for 10 min arc heat treated wrought base material and weld metal [14,15].

A separate sample was furnace-aged at 475 °C for 10 h to verify the hardness increase in B3. The hardness of the ferrite before aging was 250 ± 15 HV0.01 which increased to 375 ± 15 HV0.01 after 10 h while the hardness of austenite remained fairly constant at 265 ± 15 HV0.01. The hardness increase in this temperature range was therefore concluded to be due to 475 °C-embrittlement caused by decomposition of the ferrite [9,10].

4. Discussion

The functionally graded microstructure is discussed and findings are summarized in a schematic diagram providing mechanistic information about the content of phases, their morphologies and hardness for temperatures from the melting point to 450 °C.

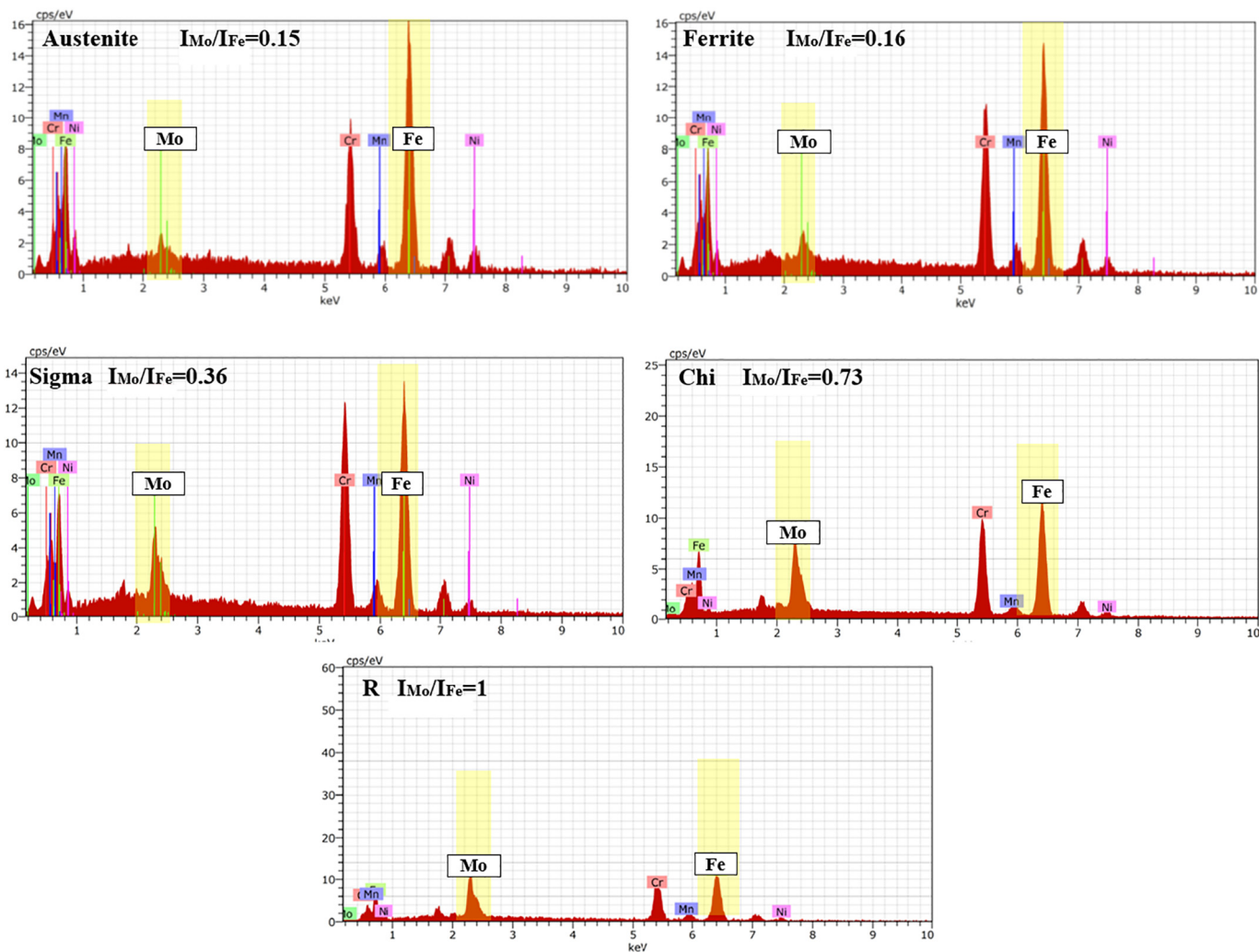


Fig. 6. EDS spectra showing detected elemental peaks measured in austenite, ferrite, σ , χ , and R, illustrating the gradual increase in Mo peak heights compared to Fe and Cr from austenite to R.

Table 3
Measured and Thermo-Calc predicted phase fractions at different temperatures.

T (°C)	δ (%)		γ (%)		σ (%)		χ (%)		R + χ + thin film (%)
	Calc.	Meas.	Calc.	Meas.	Calc.	Meas.	Calc.	Meas.	Meas.
BM	50	49.7	50	50.3	0	0	0	0	–
1200	100	100	0	0	0	0	0	0	–
1130	92.0	95 ± 2	8.0	5 ± 2	0	0	0	0	–
1090	85.7	87 ± 2	14.2	13 ± 2	0	0	0	0	–
1055	80.8	84 ± 2	19.2	16 ± 2	0	0	0	0	–
1020	77.0	82 ± 2	23.0	18 ± 2	0	0	0	0	–
1000	73.61	80.1	26.3	19.6	0	1.1	0	0	–
990	70.5	64.3	29.2	28.2	2.5	8.3	0	0.2	–
985	69	46.2	31	40.2	3.5	14.1	0	0.3	–
980	67.6	36.0	32.3	42.7	5.5	22.3	0	0.2	–
980*	23.5	–	66.2	–	9.6	–	0	–	–
950	12.3	–	69.8	–	16.5	27.0 ± 2.9	–	–	–
880	0	0.5 ± 0.2	69.8	71.3 ± 1.3	27.3	27.9 ± 1.2	0	0.2 ± 0.1	–
750	0	0.3 ± 0.1	60.3	65.0 ± 0.8	36.3	34.4 ± 0.7	2.3	0.2 ± 0.1	–
650	0	–	55.6	–	40.8	26.8 ± 4.4	0	–	1.5 ± 0.4
640	0	7.8 ± 3.6	55.2	68.3 ± 6.2	41.2	21.4 ± 2.7	0	1.1 ± 0.3	2.3 ± 0.2
630	3.6	–	51.2	–	40.7	5.4	0	–	1.9
590	26.1	–	31.8	–	38.3	0	0	–	1.6

Equilibrium phase fractions were calculated for 0% N for temperatures above 980 °C.
980* indicates phase fraction with 0.265 wt% N.

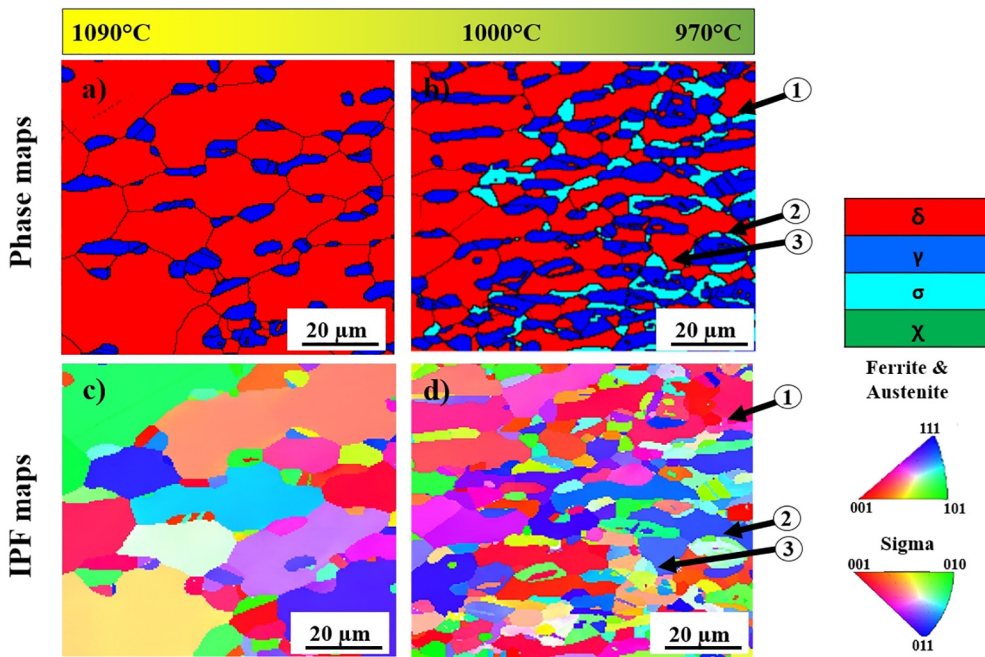


Fig. 7. EBSD phase color maps (a + b) with corresponding IPF maps (c & d). The results are for region 2 (a–c) and regions 3 (b & d) with temperatures between 1010 and 1090 °C and 970–1010 °C, respectively. Arrows 1 and 2 show two σ precipitates formed together with γ_2 while arrow 3 suggests direct transformation of δ to σ . (For interpretation of the references to color in this figure legend, the reader is referred to the web version of this article.)

4.1. Ferrite/Austenite

Fig. 12a shows that nitrogen content and temperature are two parameters governing the austenite content. The austenite content was close to that predicted for equilibrium down to temperatures of 750 °C for both nitrogen containing and free regions, including the region around the nitrogen depletion boundary.

4.1.1. Nitrogen Loss

Nitrogen loss is known to sometimes occur in welding of duplex stainless steels and is normally attributed to evaporation from the molten weld metal. In a previous study [14], it was seen that virtually all nitrogen was lost from the fusion zone of an arc heat treated sample after only 10 min. For pronounced losses from the weld pool the accompanying solid state diffusion of nitrogen towards the fusion zone will with time lead to nitrogen depletion also in the HT-HAZ. In the present study a nitrogen gradient formed between the nitrogen free molten metal and the adjacent solid material resulting in a significant nitrogen depleted region. A fully ferritic region formed above 1150 °C illustrating the critical importance of nitrogen on the phase balance in SDSS. The degree of nitrogen depletion gradually decreased with increasing distance from the fusion boundary because of slower diffusion of nitrogen at lower temperatures and the lower effective diffusion

coefficient of nitrogen in $\sigma + \gamma$ compared to in ferrite.

In actual welds, the affected region is expected to be quite narrow in most cases and therefore difficult to analyze and effects on phase balance might be difficult to distinguish from effects of thermal cycles. Nevertheless there are some reports of solid state diffusion of nitrogen in duplex and other stainless steels although not to the same extent as observed in the present study. Hosseini et al. [27] reported that an increasing number of TIG remelting passes of 2507 SDSS, with pure argon as shielding gas, decreased the nitrogen content in the melt pool and increased the fraction of nitrides in the HT-HAZ. This was attributed to nitrogen depletion resulting in less austenite reformation. Meyer et al. [28] reported nitrogen diffusion from the fusion zone into the HAZ when nitrogen containing shielding gas was used in welding of 12% chromium type EN 1.4003 ferritic stainless steels. In conclusion it can be noted that the possibility of local depletion/enrichment of nitrogen due to solid state diffusion in the HT-HAZ should not be ignored in welding. It can also be seen that the arc heat treatment technique is well suited to study this effect by applying longer remelting times.

4.1.2. Orientation Relationships

The fraction of ferrite-austenite phase boundaries obeying the KS OR increased with precipitation of secondary phases (Fig. 10). It has been reported that austenite grains precipitating in the DSS weld metal

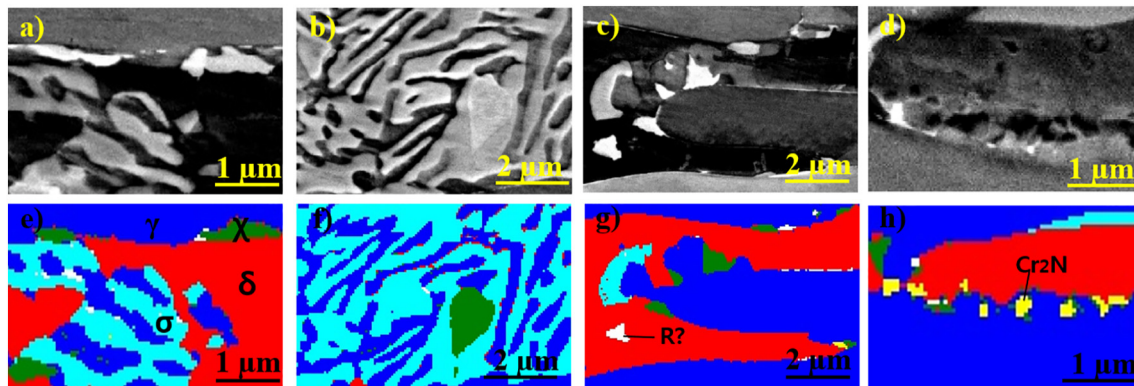


Fig. 8. SEM images with corresponding EBSD phase maps at 640 °C. (a & e) Intergranular elongated χ particles, (b & f) a χ precipitate in eutectoid $\sigma + \gamma_2$, (c & g) three discrete χ -phase precipitates and one un-indexed (white) phase, possibly R-phase, together with a region containing σ -phase and (d & h) Cr_2N formed at previous ferrite/austenite phase boundaries.

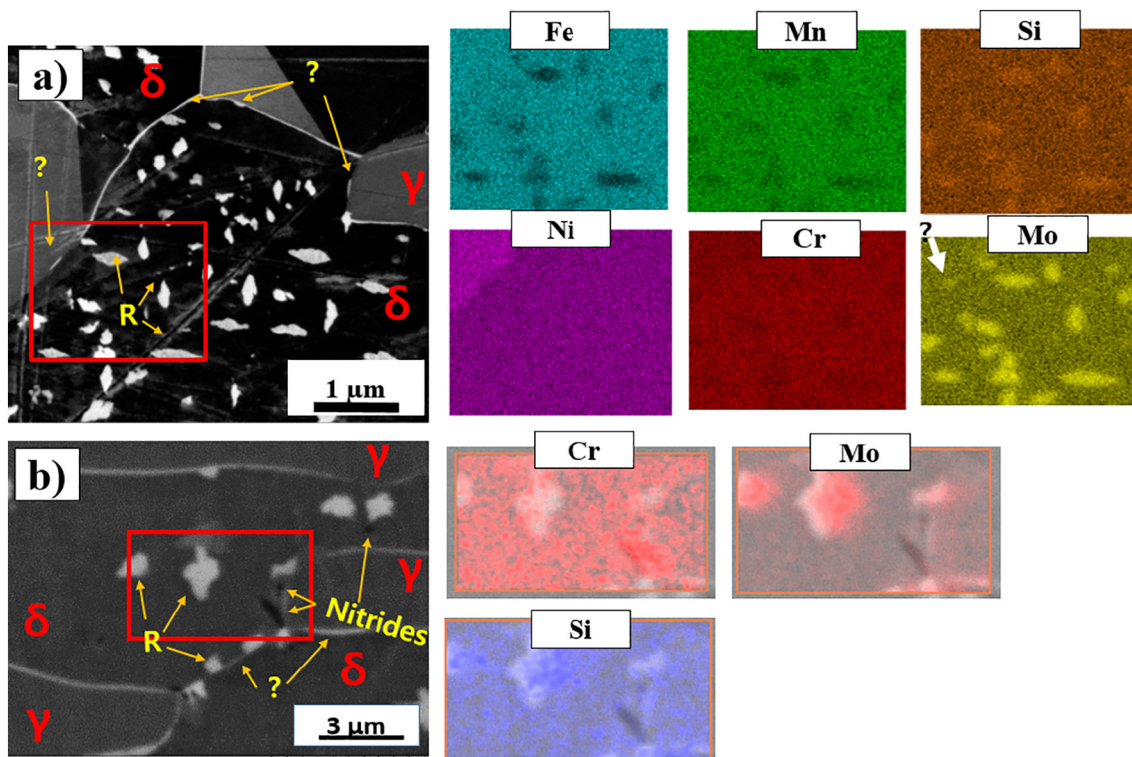


Fig. 9. BSE SEM images (a & b) and elemental EDS maps (right) for a location heat treated at 620 °C (region 7). a) Disc shaped R-phase precipitates inside a ferrite grain enriched in Mo and Si and depleted in Cr, Mn and Fe (inside the rectangle). b) Dark imaging nitride particles (arrows) on phase boundaries and adjacent to R-phase. Nitrides in the phase boundary are enriched in Cr (inside the rectangle). R-phase on the ferrite/ferrite grain boundary preferably grew into one of the adjacent ferrite grains. A Mo-rich thin film is shown by “?”.

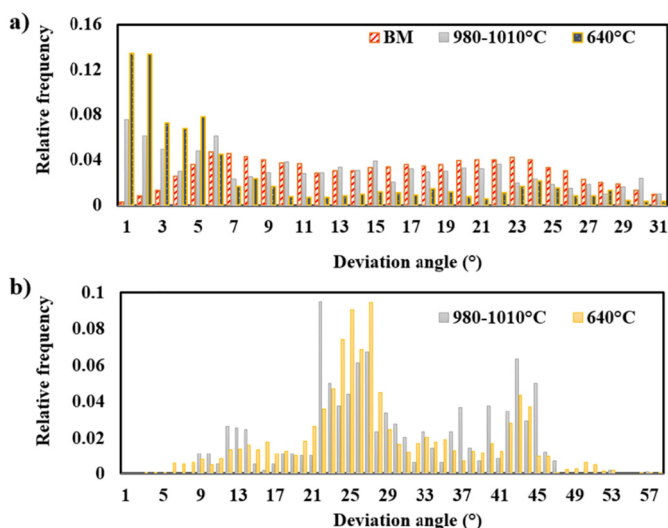


Fig. 10. a) Deviation from Kurdjumov–Sachs OR between ferrite and austenite before and after heat treatment in regions 3 and 6. b) Deviation from Chen’s OR between σ and ferrite in regions 3 and 6.

also followed KS OR [29], which is in good agreement with observations in the present study. This was due to two phenomena occurring in parallel during the arc heat treatment. Firstly, freshly formed secondary austenite (γ_2) tended to follow the KS OR. Secondly, other secondary phases, particularly σ -phase, preferentially precipitated on boundaries deviating from KS OR as also reported by Sato et al. [24], which decreased the remaining boundaries deviating from KS OR. Both are obviously effects of the strive to minimize the interfacial energy.

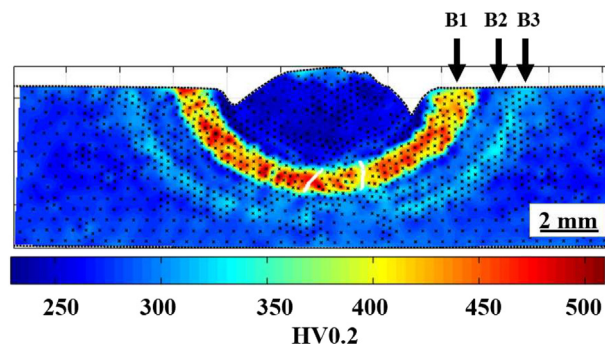


Fig. 11. Microhardness map of 10 h arc heat treated 2507 SDSS. Three bands with higher hardness can be seen; B1 at locations corresponding to aging temperatures of 680–970 °C, B2 at 590–630 °C and B3 at 450–480 °C.

4.2. Secondary Phases

4.2.1. Sigma Phase

A good agreement between the calculated and measured σ fractions was found between 750 °C and 880 °C (Table 3 and Fig. 12), where the maximum hardness of the graded microstructure was achieved due to the high hardness of σ . Nilsson et al. [30] reported that the precipitation of 40% σ in a super duplex stainless steel increased the hardness from 290 HV1 to 500 HV1, which is in good agreement with the present study. Wessman et al. [31] furthermore showed that higher fractions of σ than the calculated and measured fractions in this study were achieved after 6 months heat treatment of 2507 SDSS at 800 °C and 900 °C. Therefore, even though the calculated phase fractions are met, it does not mean that the equilibrium condition has been achieved. For shorter heat treatment times, however, the results were even further away from equilibrium conditions, as illustrated by 10 min arc heat treatment of SDSS weld metal resulting in precipitation of about 18% σ at 780 °C and a hardness of 340 HV [15]. The precipitation ranges for σ ,

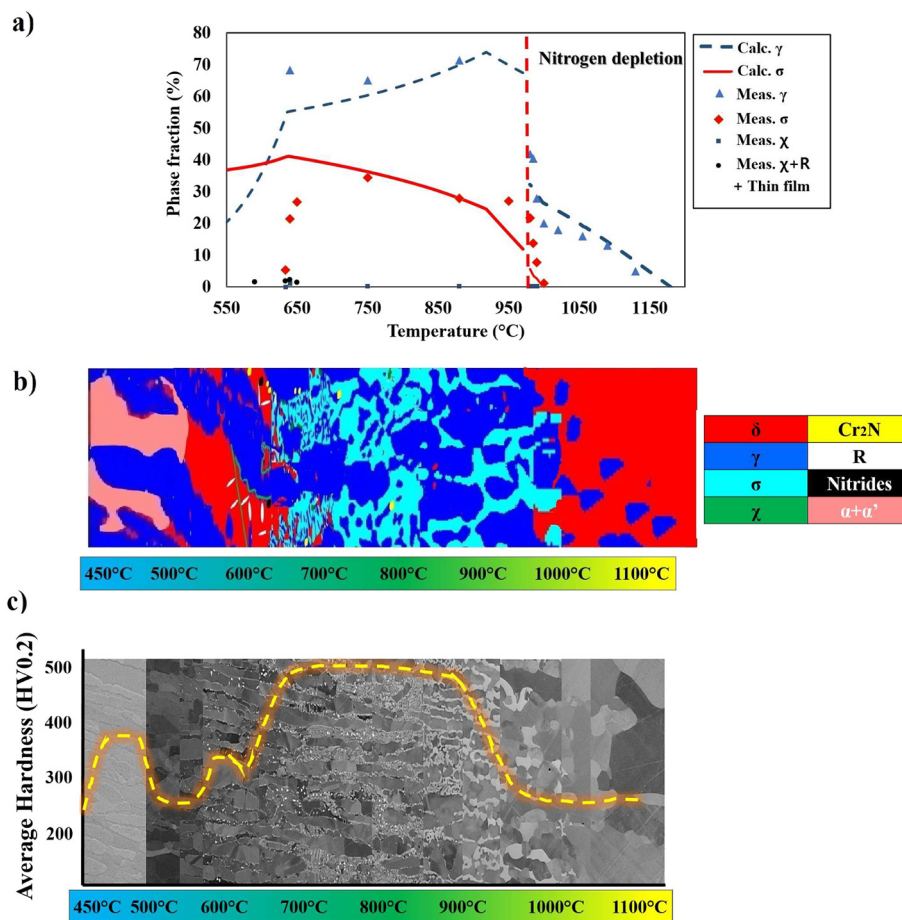


Fig. 12. a) The measured contents of γ , σ , χ and $\chi + R +$ thin film phases compared to the calculated contents predicted by thermodynamic calculations. Note that the calculated phase fractions are presented for 0 wt% N above and for 0.265 wt% N below 980 °C. b) A schematic illustration of the graded SDSS microstructure showing phases and their typical morphologies. c) Average hardness as a function of temperature on a background composed of representative BSE SEM images.

in addition, after the 10 min arc heat treatment were between 700 and 1020 °C for weld metal [15] and 750–1010 °C for wrought base material [14] as compared to the range of 630–1010 °C for 10 h heat treatment. This indicates that longer heat treatment time widened the σ precipitation temperature range, particularly to lower temperatures.

As shown in Fig. 12, the difference between measured and predicted σ content above 950 °C suggests that the thermodynamic calculations underestimate the σ content at the upper limit of the σ stability temperature range. For the same alloy, Pardal et al. [32] reported that 25% σ precipitated after 125 min aging at 950 °C, which is very close to the 27.0% measured in the current study. Dos Santos et al. [33] also reported the same trend as shown in Fig. 12, for a 2205 DSS. Below 750 °C, furthermore, a longer time would be needed to approach the equilibrium content, as also reported by Dos Santos et al. [33] for type 2205 DSS, and the discrepancy at lower temperatures is therefore expected.

Four possible mechanisms of σ formation were identified in this study: 1) Direct transformation of ferrite to σ (Fig. 7d): In this case σ consumes ferrite, in line with observations made by Gunn [5]. 2) Eutectoid transformation of ferrite to σ and γ_2 (Fig. 7d): Cooperative growth of σ and γ_2 with γ_2 growing epitaxially on primary austenite. 3) Transformation of austenite to σ . 4) Transformation of χ and R-phase to σ .

The two last mechanisms need further explanations. The measured and calculated phase contents at 640 °C showed that the calculated σ content would not be met even if all remaining ferrite (7%) would transform to σ . Dos Santos et al. [34], Nilsson et al. [20] and Hwang et al. [13] reported the transformation of austenite, χ or R-phase to σ in duplex stainless steels, respectively, which could be the missing links required to achieve the calculated σ content at this temperature. This is supported by the fact that the measured austenite content was higher

than the calculated one and transformation of austenite to σ would thereby shift the phase balance towards the equilibrium condition.

Blocky and coral shape σ morphologies (Fig. 4) were observed at high and low temperatures, respectively. A finer coral-shape σ at lower temperatures has been observed in austenitic stainless steels by Perron et al. [35], in DSS wrought by Zhang et al. [36] and in SDSS weld metal by Hosseini et al. [15]. It has been claimed that a larger number of σ nuclei at lower temperatures is the main reason of the coral-shape morphology [34]. The shape could also be explained in terms of how σ -phase grows. Diffusion is obviously slower at lower temperatures, which causes a more pronounced super saturation of surrounding ferrite in austenite stabilizing elements as σ grows. This facilitates formation of a finer austenite between σ precipitates. Caballero et al. [37] reported that the reduction of pearlite lamellar spacing at lower transformation temperatures in carbon steels is due to the temperature dependent diffusion rate, which is analogous to the present observation. Zhang et al. [36] also noted the similarity between pearlite growth in carbon steel and coral shape (cellular) σ growth in a hyper duplex stainless steel. It can therefore be concluded that a combination of nucleation [34] and cooperative eutectoid growth [36] governs σ morphology at lower temperatures.

4.2.2. Chi Phase

The maximum amount of χ was observed outside the stability temperature range (predicted with JMatPro) at temperatures where also the σ -phase content deviates from the calculated fraction. Hence, the microstructure has not approached the equilibrium condition below 750 °C. Consequently, χ is not a stable phase and is expected to disappear for longer holding times, most likely by transforming to σ as reported by Nilsson et al. [20]. Dos Santos et al. [33] investigated a type 2205 DSS at 700–900 °C and found the maximum content of χ at 700 °C

after 10 h, which disappeared after longer heat treatment.

4.2.3. R-phase

R-phase with different sizes and morphologies was observed as shown in Fig. 9 and illustrated schematically in Fig. 12b. R-phase usually forms at ferrite/ferrite and ferrite subgrain boundaries but can also form intragranularly, having disc-shape morphologies [38,39]. Hwang et al. [13] reported that R-phase precipitated more rapidly than σ at 600 °C, which is in good agreement with the present study. The precipitation of R-phase is also believed to be the cause of the increased hardness around 600 °C (B2 in Fig. 11). R-phase has been reported to have an OR with the ferrite as follows: $(0001)_R // (111)_\delta$ and $[2\bar{1}10]_R // [1\bar{3}2]_\delta$ [38]. This is in line with the observation of two perpendicularly oriented families of precipitates in the present study (Fig. 9a). The internal structure of R is heavily faulted which causes high lattice strains in the vicinity in the ferrite matrix which has been suggested to lead to enhanced localized corrosion and may facilitate stress corrosion cracking [38,39].

4.2.4. Nitrides

The typical locations of Cr_2N particles are schematically illustrated in Fig. 12b. Nitrides mostly precipitated at austenite-ferrite boundaries and were then embedded inside the austenite grains by epitaxial γ_2 growth on the primary austenite grains. Zhang et al. [36] observed nitrides at the same locations in a hyper duplex stainless steels heat treated at 950 °C. The predicted and observed temperature ranges of Cr_2N precipitation, are in good agreement. Some of the precipitates shown as black in the schematic microstructure could, however, be π . Nilsson et al. [40] reported the precipitation of π as also predicted by thermodynamic calculations with JMatPro for temperatures below 600 °C. CrN, although not predicted by thermodynamic calculations, has also been reported to form in duplex stainless steel [11] but could not be identified in this study.

4.2.5. Thin Films on δ/γ and δ/δ Boundaries

The presence of thin films on most of the δ/γ and δ/δ boundaries in region 7 and some δ/γ boundaries in region 6 implies either segregation of alloying elements or precipitation. Karlsson et al. [12] and Hosseini et al. [15] reported similar films forming in DSS weld metals. Otárola et al. observed the precipitation of very small σ and χ on δ/γ phase boundaries at the same temperatures [41]. Escriba et al. also observed the precipitation of continuous χ film on δ/γ and δ/δ boundaries in 2205 DSS prior to the formation of σ at 700 °C and 750 °C [42]. Zhang et al. [43] reported the segregation of Mo and C on δ/γ after heat treatment of a cast DSS at 400 °C and Örnek et al. [39] also found thin film like carbides on δ/γ and δ/δ boundaries in 2205 DSS heat treated at 475 °C. Further investigations are however needed to clarify the nature of the thin films.

4.3. Graded Structure Functionality

Properties of all materials are a direct function of their microstructure including features such as phase fractions, phase morphology, grain size, etc. This is also true in a graded material but here the combination of the many local microstructures with their specific properties determine the overall properties. The evaluation of a graded microstructure can be used either as first step in an attempt to find the optimum condition for achieving a specific set of properties or to understand overall properties as an effect of combining local properties. In either case a specific property that can be evaluated on a local level needs to be mapped to infer other properties. In duplex stainless steels, the hardness increase due to the presence of secondary phases (particularly σ and R-phase) is an important indication of a significant loss of toughness [12]. In addition, the degree of sensitization is known to increase with increasing content of intermetallic phases such as σ and R-phase [12,44]. Therefore, lower impact toughness and poor corrosion

resistance are expected at temperatures between 560 °C and 1100 °C, where high hardness and secondary phases were observed.

As seen in Fig. 11a, a significant hardness increase was also observed in locations corresponding to temperatures of 450–480 °C. Hardness testing is commonly used to detect so-called 475 °C-embrittlement caused by decomposition of ferrite to Cr-rich (α') and Fe-rich ferrite (α) [9,10]. The increased hardness therefore strongly suggests decomposition of ferrite although on a too fine scale to be observed with SEM. Tavares et al. [45] reported the same hardness as that obtained in the current study for 2507 SDSS after 10 h heat treatment at 475 °C. A 50% drop of impact toughness has also been reported to occur in < 6 min in 2507 SDSS at this temperature [3]. The etching response of ferrite and austenite in this region was very similar resulting in poor contrast in LOM micrographs (Fig. 4). Örnek et al. [46] reported that the Volta potential was the same for ferrite, austenite and phase boundaries in a DSS heat treated for 5 h at 475 °C. However, there was a difference after 20 h heat treatment. Örnek et al. [46] suggested that the potential of the ferrite, and thereby the etching response, is related to the size of α' and therefore will depend on aging time. The etching response in the studied SDSS sample is therefore interpreted as being related to formation of α' .

Both in the case of precipitation of intermetallics and for decomposition of ferrite to Cr-rich (α') and Fe-rich ferrite (α) it is clear that properties are affected by the local microstructure in the graded material. One way of illustrating the correlation between microstructure and the functionality of the graded material is, as shown in Fig. 12c, by mapping the resulting hardness as a function of heat treatment temperature.

5. Conclusions

A functionally graded microstructure was produced by the arc heat treatment of grade 2507 (UNS S32750) super duplex stainless steel under steady state conditions for 10 h. Microstructural analyses were performed and experimental results were compared to thermodynamic calculations.

- Nitrogen was depleted up to 1.2 mm from the fusion boundary by solid state diffusion. This affected the ferrite/austenite balance and resulted in the formation of a fully ferritic microstructure in the region heat treated between 1150 °C and 1430 °C.
- Sigma phase formed between 630 °C and 1000 °C, chi phase at 560–1000 °C, chromium nitrides at 600–900 °C, R-phase at 560–660 °C, and presumably Mo-rich thin intergranular films at 560–660 °C.
- Evaluation of phase fractions in the graded microstructure revealed that equilibrium sigma and austenite fractions, as predicted by thermodynamic calculations, were approached at 750–880 °C, but not above 950 °C or below 750 °C.
- The morphology of constituents of the graded microstructure changed with decreasing temperature. In particular, the sigma phase morphology changed from being blocky to coral like and chi phase from blocky to elongated particles in phase boundary regions.
- Secondary austenite obeyed mostly the Kurdjumov–Sachs orientation relationship (OR) with ferrite, and chi phase had a cube-on-cube OR with ferrite, while no specific OR could be identified for sigma phase.
- The functionally graded material showed a clear correlation between secondary phase fractions and local hardness with an increased hardness in locations corresponding to sigma, R-phase and chi precipitation as well as to heat treatment temperatures of 450–480 °C, correlating to the well-known 475 °C-embrittlement, being related to the decomposition of ferrite which also produced a different etching response.
- A schematic diagram linking phase contents, their morphologies and hardness, as a function of exposure temperature, is introduced.

Acknowledgement

The financial support from the KK-foundation for the research school SiCoMaP (20140130) and the DUWELTOOL project (2016-02834) funded by Vinnova is acknowledged. Authors would like to thank Dr. Matthew Roy and Mr. Daniel Wilson for their assistance with automatic hardness testing, Mr. Kjell Hurtig and Mr. Jonas Olsson for performing heat treatments and Outokumpu AB for providing test material.

References

- [1] J.-O. Nilsson, G. Chai, The physical metallurgy of duplex stainless steels, Duplex Stainless Steel Conference, Beaune, France, 2010.
- [2] J.-O. Nilsson, Super duplex stainless steels, *Mater. Sci. Technol.* 8 (8) (1992) 685–700.
- [3] Handbook of Stainless Steel, Outokumpu Oyj, Finland, 2013.
- [4] R. Pettersson, E. Johansson, Stress corrosion resistance of duplex grades, Duplex World, 2010.
- [5] R.N. Gunn, Duplex Stainless Steels: Microstructure, Properties and Applications, Woodhead Publishing, 1997.
- [6] M. Pohl, O. Storz, T. Glogowski, Effect of intermetallic precipitations on the properties of duplex stainless steel, *Mater. Charact.* 58 (1) (2007) 65–71.
- [7] L. Karlsson, S. Rigdal, S. Pak, Effects of Intermetallic Phases in Duplex Stainless Steels Weldments Duplex America 2000, (2000), p. 15.
- [8] A. Redjaimia, G. Metauer, M. Gantois, Decomposition of delta ferrite in an Fe-22 Cr-5 Ni-3 Mo-0.03 C Duplex stainless steel. A morphological and structural study, Duplex Stainless Steels'91, vol. 1, 1991, pp. 119–126.
- [9] C. Örnek, D. Engelberg, S. Lyon, T. Ladwein, Effect of “475 °C Embrittlement” on the Corrosion Behaviour of Grade 2205 Duplex Stainless Steel Investigated Using Local Probing Techniques, Corrosion Management, The Institute of Corrosion, Northampton, 2013, pp. 9–11.
- [10] C. Örnek, S.A. Idris, P. Reccagni, D.L. Engelberg, Atmospheric-induced stress corrosion cracking of grade 2205 duplex stainless steel—effects of 475 °C embrittlement and process orientation, *Metals* 6 (7) (2016) 167.
- [11] C. Örnek, D.L. Engelberg, Correlative EBSD and SKPFM characterisation of microstructure development to assist determination of corrosion propensity in grade 2205 duplex stainless steel, *J. Mater. Sci.* 51 (4) (2016) 1931–1948.
- [12] L. Karlsson, L. Ryen, S. Pak, Precipitation of intermetallic phases in 22% Cr duplex stainless weld metals, *Weld. J.* 74 (1) (1995) 28–38.
- [13] T. Hwang, J. Kim, K. Kim, W. Moon, C. Kang, Effect of R-phase on impact toughness of 25Cr-7Ni-4Mo super duplex stainless steel, *Met. Mater. Int.* 20 (1) (2014) 13–17.
- [14] V.A. Hosseini, L. Karlsson, K. Hurtig, I. Choquet, D. Engelberg, M.J. Roy, C. Kumara, A novel arc heat treatment technique for producing graded microstructures through controlled temperature gradients, *Mater. Des.* 121 (2017) 11–23.
- [15] V.A. Hosseini, L. Karlsson, D. Engelberg, S. Wessman, Time-temperature-precipitation and property diagrams for super duplex stainless steel weld metals, *Weld. World* (2018), <http://dx.doi.org/10.1007/s40194-018-0548-z>.
- [16] C. Örnek, D. Engelberg, Towards understanding the effect of deformation mode on stress corrosion cracking susceptibility of grade 2205 duplex stainless steel, *Mater. Sci. Eng. A* 666 (2016) 269–279.
- [17] P. Cizek, The microstructure evolution and softening processes during high-temperature deformation of a 21Cr-10Ni-3Mo duplex stainless steel, *Acta Mater.* 106 (2016) 129–143.
- [18] C.U. Jeong, W. Woo, J.Y. Choi, S.H. Choi, Effect of kinematic stability of initial orientation on deformation heterogeneity and ductile failure in duplex stainless steel during uniaxial tension, *Acta Mater.* 67 (2014) 21–31.
- [19] L.D. Bobbio, R.A. Otis, J.P. Borgonia, R.P. Dillon, A.A. Shapiro, Z.-K. Liu, A.M. Beese, Additive manufacturing of a functionally graded material from Ti-6Al-4V to Invar: experimental characterization and thermodynamic calculations, *Acta Mater.* 127 (2017) 133–142.
- [20] J. Nilsson, A. Wilson, Influence of isothermal phase transformations on toughness and pitting corrosion of super duplex stainless steel SAF 2507, *Mater. Sci. Technol.* 9 (7) (1993) 545–554.
- [21] V.A. Hosseini, S. Wessman, K. Hurtig, L. Karlsson, Nitrogen loss and effects on microstructure in multipass TIG welding of a super duplex stainless steel, *Mater. Des.* 98 (2016) 88–97.
- [22] C. Kumara, Modelling of the Temperature Field in TIG Arc Heat Treated Super Duplex Stainless Steel Samples, Engineering, University West, Sweden, 2016.
- [23] G. Gutiérrez-Vargas, V.H. López, H. Carreón, J.-Y. Kim, A. Ruiz, ACPD detection and evaluation of 475 °C embrittlement of aged 2507 super duplex stainless steels, AIP Conference Proceedings, AIP Publishing, 2017, p. 110018.
- [24] Y.S. Sato, H. Kokawa, Preferential precipitation site of sigma phase in duplex stainless steel weld metal, *Scr. Mater.* 40 (6) (1999) 659–663.
- [25] T. Chen, J. Yang, Effects of solution treatment and continuous cooling on σ -phase precipitation in a 2205 duplex stainless steel, *Mater. Sci. Eng. A* 311 (1) (2001) 28–41.
- [26] T.-H. Lee, H.-Y. Ha, B. Hwang, S.-J. Kim, Isothermal decomposition of ferrite in a high-nitrogen, nickel-free duplex stainless steel, *Metall. Mater. Trans. A* 43 (3) (2012) 822–832.
- [27] V.A. Hosseini, M.A.V. Bermejo, J. Gårdstam, K. Hurtig, L. Karlsson, Influence of multiple thermal cycles on microstructure of heat-affected zone in TIG-welded super duplex stainless steel, *Weld. World* 60 (2) (2016) 233–245.
- [28] A. Meyer, M.D. Toit, Interstitial diffusion of carbon and nitrogen into heat-affected zones of 11–12% chromium steel welds, *Weld. J.* 80 (12) (2001) (275-s).
- [29] L. Karlsson, H. Arcini, E.-L. Bergquist, J. Weidow, J. Börjesson, Effects of alloying concepts on ferrite morphology and toughness of lean duplex stainless steel weld metals, *Weld. World* 54 (11–12) (2010) R350–R359.
- [30] J.-O. Nilsson, P. Kangas, A. Wilson, T. Karlsson, Mechanical properties, microstructural stability and kinetics of σ -phase formation in 29Cr-6Ni-2Mo-0.38N superduplex stainless steel, *Metall. Mater. Trans. A* 31 (1) (2000) 35–45.
- [31] S. Wessman, R. Pettersson, S. Hertzman, On phase equilibria in duplex stainless steels, *Steel Res. Int.* 81 (5) (2010) 337–346.
- [32] J.M. Pardal, S.S.M. Tavares, M.d.P.C. Fonseca, J.A.d. Souza, L.M. Vieira, H.F.G.d. Abreu, Deleterious phases precipitation on superduplex stainless steel UNS S32750: characterization by light optical and scanning electron microscopy, *Mater. Res.* 13 (3) (2010) 401–407.
- [33] D.C. Dos Santos, R. Magnabosco, Kinetic study to predict sigma phase formation in duplex stainless steels, *Metall. Mater. Trans. A* 47 (4) (2016) 1554–1565.
- [34] D.C.d. Santos, R. Magnabosco, C. de Moura-Neto, Influence of sigma phase formation on pitting corrosion of an aged UNS S31803 duplex stainless steel, *Corrosion* 69 (9) (2013) 900–911.
- [35] A. Perron, C. Toffolon-Masclat, X. Ledoux, F. Buy, T. Guilbert, S. Urvoy, S. Bosonnet, B. Marini, F. Cortial, G. Texier, C. Harder, V. Vignal, P. Petit, J. Farré, E. Suzon, Understanding sigma-phase precipitation in a stabilized austenitic stainless steel (316Nb) through complementary CALPHAD-based and experimental investigations, *Acta Mater.* 79 (2014) 16–29.
- [36] B. Zhang, Z. Jiang, H. Li, S. Zhang, H. Feng, H. Li, Precipitation behavior and phase transformation of hyper duplex stainless steel UNS S32707 at nose temperature, *Mater. Charact.* 129 (2017) 31–39.
- [37] F. Caballero, C. Capdevila, C.G. de Andrés, Modeling of the interlamellar spacing of isothermally formed pearlite in a eutectoid steel, *Scr. Mater.* 42 (6) (2000) 537–542.
- [38] A. Redjaimia, J. Morniroli, P. Donnadieu, G. Metauer, Microstructural and analytical study of heavily faulted Frank-Kasper R-phase precipitates in the ferrite of a duplex stainless steel, *J. Mater. Sci.* 37 (19) (2002) 4079–4091.
- [39] C. Örnek, M. Burke, T. Hashimoto, J. Lim, D. Engelberg, 475 °C embrittlement of duplex stainless steel—a comprehensive microstructure characterization study, *Mater. Perform. Charact.* 6 (3) (2017) 409–436.
- [40] J.-O. Nilsson, P. Liu, Aging at 400–600 °C of submerged arc welds of 22Cr-3Mo-8Ni duplex stainless steel and its effect on toughness and microstructure, *Mater. Sci. Technol.* 7 (9) (1991) 853–862.
- [41] T. Otárola, S. Hollner, B. Bonnefois, M. Anglada, L. Coudreuse, A. Mateo, Embrittlement of a superduplex stainless steel in the range of 550–700 °C, *Eng. Fail. Anal.* 12 (6) (2005) 930–941.
- [42] D.M. Escriba, E. Materna-Morris, R.L. Plaut, A.F. Padilha, Chi-phase precipitation in a duplex stainless steel, *Mater. Charact.* 60 (11) (2009) 1214–1219.
- [43] B. Zhang, F. Xue, S. Li, X. Wang, N. Liang, Y. Zhao, G. Sha, Non-uniform phase separation in ferrite of a duplex stainless steel, *Acta Mater.* 140 (2017) 388–397.
- [44] J. Hong, D. Han, H. Tan, J. Li, Y. Jiang, Evaluation of aged duplex stainless steel UNS S32750 susceptibility to intergranular corrosion by optimized double loop electrochemical potentiokinetic reactivation method, *Corros. Sci.* 68 (2013) 249–255.
- [45] S. Tavares, A. Loureiro, J. Pardal, T. Montenegro, V. da Costa, Influence of heat treatments at 475 and 400 °C on the pitting corrosion resistance and sensitization of UNS S32750 and UNS S32760 superduplex stainless steels, *Mater. Corros.* 63 (6) (2012) 522–526.
- [46] C. Örnek, J. Walton, T. Hashimoto, T. Ladwein, S. Lyon, D. Engelberg, Characterization of 475 °C embrittlement of duplex stainless steel microstructure via scanning kelvin probe force microscopy and magnetic force microscopy, *J. Electrochem. Soc.* 164 (6) (2017) C207–C217.